General approach for efficient prediction of refrigeration performance in caloric materials

Xiong Xu, Weifeng Xie, Fangbiao Li, Chang Niu, Min Li, and Hui Wang[*]
School of Physics, Hunan Key Laboratory of Super Microstructure and Ultrafast Process, Hunan Key Laboratory of Nanophotonics and Devices, State Key Laboratory of Powder Metallurgy, Central South University, Changsha 410083, China

(Received 10 July 2023; revised 8 June 2024; accepted 21 June 2024; published 15 July 2024)

Solid-state refrigeration holds promise for environmentally friendly cooling with high energy efficiency and downsize scalability. However, its refrigeration performance is notably inferior in comparison with commercial refrigerants due to the lack of scientific guidance for material discovery and performance improvement. Here, we provide an efficient approach to investigate caloric effect under external factors (i.e., electric fields, magnetic fields, and mechanical fields). Using the electrocaloric material $PbTiO_3$ (PTO) as a prototype and employing *ab initio* calculations combined with deep potential machine learning, we demonstrate the field-dependent isothermal entropy change ΔS and adiabatic temperature change ΔT, along with the coefficient of performance near the phase transitions temperature (T_c). Through analysis of the evolution of microscopic dynamics, we clarify that the refrigeration process involves heat absorption by a transition from a low-potential-energy to a high-potential-energy state. This transition, in a more general case, can be defined as a conventional caloric effect driven by temperature when $T > T_c$, or an inverse caloric effect driven by external field when $T < T_c$. Importantly, this approach is successfully applied to magnetocaloric, elastocaloric, and barocaloric materials, from which we further showcase the regulation of caloric effect in multicaloric refrigeration process. This work establishes an effective and universal method for predicting key refrigeration parameters, which can be applied to extensive caloric materials, that provide important insights for material design in solid-state cooling technology.

DOI: 10.1103/PhysRevApplied.22.014036

I. INTRODUCTION

Currently, traditional vapor-compression refrigeration technology is widely used around the world in refrigerators and air conditioners, consuming large amounts of electrical energy and causing extensive greenhouse effects that are thousands of times larger than those due to carbon dioxide emissions. With increasing attention being paid to environmental protection and energy utilization, it is urgent and imperative to seek more efficient and environmentally friendly refrigeration technology. In recent years, solid-state refrigeration technology based on the magnetocaloric effect (MCE, induced by magnetic fields) [1–7], electrocaloric effect (ECE, induced by electric fields) [8–14], elastocaloric effect (eCE, induced by uniaxial stress) [15–19], and barocaloric effect (BCE, induced by hydrostatic pressure) [20–29] has received tremendous attention, as it promises green forms of refrigeration and downsizes scalability with high efficiency.

The key parameters for evaluating solid-state refrigeration performance include adiabatic temperature change, ΔT, and isothermal entropy change, ΔS. Traditionally, three methods are employed to determine ΔS and ΔT in caloric effect: direct, quasidirect, and indirect [30]. The direct approach allows for the direct measurement of ΔS and ΔT under isothermal or adiabatic conditions, which is desirable but technically challenging, requiring highly sensitive temperature sensors with ultrashort response times [10]. In the quasidirect method, obtaining the temperature dependence of heat flow involves repeating measurements at various temperatures during both cooling and heating. However, due to thermal conduction, stabilizing temperature requires a prolonged waiting period, making the process time-consuming [31]. Additionally, unavoidable thermal contact between the sample and the differential scanning calorimetry sensor leads to heat losses [32–34]. The accuracy and reliability of indirect methods using Maxwell's relation and the Clausius-Clapeyron equation are significantly affected by sampling frequency and noise. Challenges persist in precisely determining the caloric effect in materials undergoing first-order phase transitions using current indirect techniques [1]. The lack of advanced experimental techniques and effective theoretical approaches led to a serious lack of scientific guidance for precise material design and performance improvement,

---

[*] Contact author: huiwang@csu.edu.cn

thereby impeding the widespread application of solid-state cooling technology.

In this work, we propose to calculate caloric effect by solely requiring the potential energy difference (PED) between the initial and final states, as well as the work done by an external field, rather than simulating the complicated phase-transition process that accompanies it with the evolution of order parameters. Specifically, the formula for calculating entropy change is as follows:

$$\Delta S(T, y_0 \rightarrow y_1) = \frac{\Delta U^{\mathrm{pot}}|_{y_0}^{y_1} - W_Y}{T}, \tag{1}$$

where $\boldsymbol{Y}$ represents the generalized force, which can be in the form of a magnetic field, electric field, or mechanical field, and y is the generalized coordinate corresponding to the order parameter of the field. Moreover, $\Delta U^{\mathrm{pot}}|_{y_0}^{y_1}$ is the PED from y_0 to y_1; W_Y is the work done by the external field from y_0 to y_1. This method has been validated through systematic comparisons with experimental data and indirect methods based on the Maxwell relations, which can be extended to a more comprehensive study of field-induced caloric effects, encompassing magnetocaloric, electrocaloric, elastocaloric, barocaloric materials, and even multicaloric materials. It is noteworthy that the efficiency of this method is one to two orders of magnitude faster than conventional methods, holding promise for application in machine learning-assisted high-throughput screening of caloric materials with superior refrigeration performance.

II. RESULTS AND DISCUSSION

Based on a deep learning potential (DP) model [35–37] and modern polarization theory [38] (see the METHODS section), we typically use $PbTiO_3$ (PTO) as an example and directly elucidate the microscopic dynamics of electrocaloric refrigeration and trace the evolution of system state functions during adiabatic and isofield processes. We compared the energy and atomic forces of the DP and density functional theory (DFT) on a test dataset at different temperatures (ranging from 300 to 900 K) to verify the transferability and reliability of the potential function. Our results indicate a good agreement between the energies and forces calculated by DP and DFT, with an average absolute error of 0.43 meV per atom and 0.038 eV/Å, respectively, as illustrated in Figs. 1(a) and 1(b). Moreover, the DP model effectively replicates the anharmonic double-well potential, a crucial indicator of ferroelectric phase transitions, as depicted in Fig. 1(c). The phonon dispersion spectrum is a quantum mechanical description

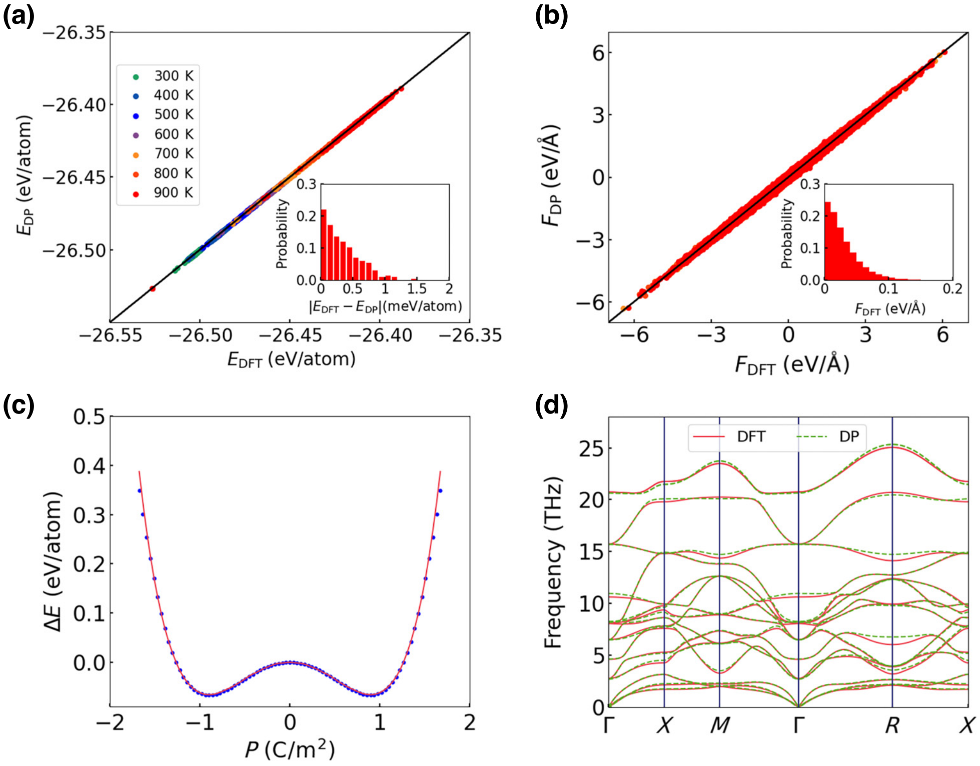

FIG. 1. Comparison of (a) energies and (b) atomic forces calculated by the DP model and DFT at different temperatures. (c) Double-well potential versus polarization P computed by DFT (red lines) and DP (blue dots). (d) Phonon dispersion relations of the P4mm structure were calculated using DFT (red lines) and DP (green dotted lines).

of atomic vibrations along different wave vectors, where atomic forces play a vital role. The precise calculation of phonon dispersion serves as a rigorous standard to test the accuracy of the DP method. We computed the phonon spectra of the P4mm phase using DFT and deep potential molecular dynamics (DPMD), employing the frozen phonon approach as implemented in the open-source package PHONOPY [39,40], which has been used in various other systems [41,42]. As shown in Fig. 1(d), the DPMD phonon spectrum of the P4mm phase closely aligns with the DFT calculations, demonstrating that our well-trained DP potential can be utilized for molecular dynamics simulations with DFT accuracy.

The characterization of the ferroelectric phase transitions and the temperature-dependent variation of polarization under external fields are crucial for assessing the magnitude of the ECE. Figure 2(a) illustrates the temperature-dependent lattice parameters of PTO, where the red line represents the DPMD result, and the blue line denotes the experimental data [43]. The DPMD result is basically consistent with the experimental data, with discrepancies in lattice parameters and volume within an acceptable range (average value within 1%). One may note that PTO undergoes an abrupt transition from P4mm to Fm-3m phase with a prominent decrement of volume at ∼760 K, in good agreement with the experimental value [43]. Moreover, we successfully reproduced the pressure-induced phase transition of PTO at room temperature, as shown in Fig. 2(b). As the pressure increases, both lattice parameters c and a gradually decrease and the tetragonal-to-cubic phase transition occurs at 10 GPa, which is closely consistent with experimental observations [44,45]. The polarization does not vanish until the pressure reaches 12 GPa in accordance with the ferroelectric-to-paraelectric transition reported in the Raman measurements [46]. It is noteworthy, in LAMMPS [47], that the heat capacity C was assigned the value $3Nk_\mathrm{B}$ [black dashed line in Fig. 2(c)], while the experimentally reported [48] heat capacity C values are indicated by the green dots in Fig. 2(c). Using the Debye model to fit the experimental values [49], we obtained the curve of the C variation with temperature as shown by the blue curve in Fig. 2(c). There is a noticeable discrepancy $\int_0^T C_\mathrm{lammps} dT \neq \int_0^T C_\mathrm{exp} dT$, indicating that, at the same elevated temperature, the heat absorbed in the LAMMPS simulation is greater than the actual heat absorbed, suggesting that the simulated temperature in LAMMPS is lower than the actual temperature. Therefore, we applied a temperature correction using the formula $\int_0^{T_\mathrm{lammps}} C_\mathrm{lammps} dT = \int_0^{T_\mathrm{exp}} C_\mathrm{exp} dT$.

In addition, we simulated the temperature-dependent ferroelectric hysteresis loop of PTO, a crucial aspect for comprehending ferroelectric polarization and further assessing the ECE, as shown in Fig. 3(a). Notably, the coercive electric field decreases from 2.4 MV/cm at 300 K to 0.2 MV/cm at 700 K, and the spontaneous polarization decreases from 0.86 C/m^2 at 300 K to 0.58 C/m^2 at 700 K. Furthermore, we simulated the temperature-dependent polarization under different electric fields, as depicted in Fig. 3(b). Beyond the Curie temperature T_c, PTO transitions into the paraelectric phase with a spontaneous polarization of $P_s = 0$. With an increasing electric field strength, T_c gradually ascends from 760 K at 0 MV/cm to approximately 1000 K at 1 MV/cm. It is well-established that the Grüneisen parameter, which can be defined as

$$\Gamma_E = -\frac{1}{C_E}\left(\frac{\partial P}{\partial T}\right)_E,$$

in the ECE is the appropriate quantity to quantify caloric effects because it can be expressed as $\Gamma_E = 1/T(\partial T/\partial E)_S = -(1/C_E)(\partial S/\partial E)_T$ [50–52]. In this paper, we adopt the heat capacity from the results displayed in Fig. 2(c). We disregard the impact of external fields on heat capacity, as discussed in previous work [53]. Figure 3(c)

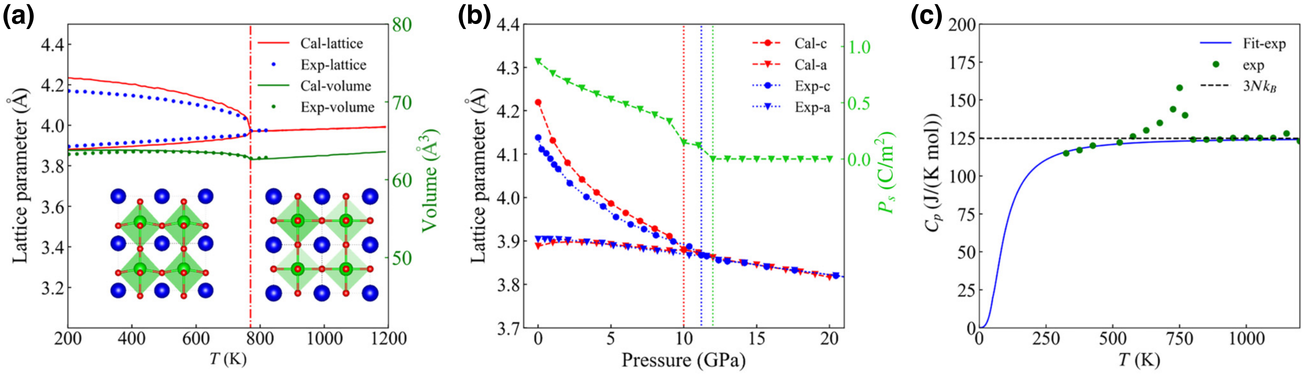

FIG. 2. (a) Temperature-dependent lattice parameters and volume. Insets provide the structure of the P4mm phase and Fm-3m phase. (b) Pressure-induced phase transition of PTO at room temperature. (c) Temperature-dependent specific heat (the black dotted line represents $C_\mathrm{lammps} = 3Nk_B$, the green dot signifies the experimental value, and the blue line denotes the specific heat fitted by the Debye model).

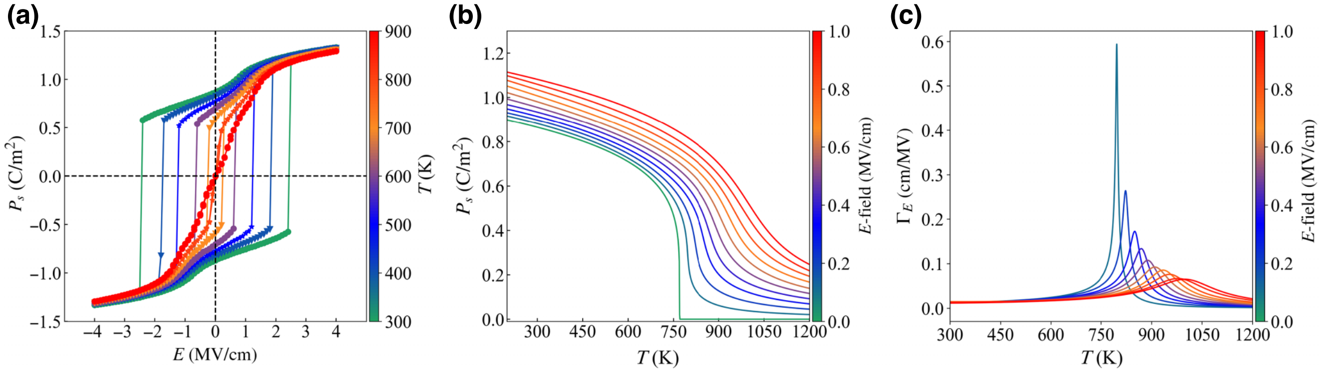

FIG. 3. (a) Ferroelectric hysteresis loop of PTO for different temperatures and (b) temperature-dependent polarization under varying electric fields. (c) The Grüneisen parameter for different temperatures under varying electric fields.

illustrates the variation of Γ_E under different electric fields and temperatures. It is observable that near T_c, a relatively small electric field can produce a significant peak in Γ_E, which greatly contributes to the electrocaloric effect. However, as the temperature rises, the electric field required to achieve the peak value increases and the magnitude of the Γ_E peak also gradually decreases. This indicates that a higher temperature necessitates a greater electric field to generate an electrocaloric effect of the same magnitude.

In Fig. 4, we depict the electrocaloric refrigeration process of PTO at 800 K and atmospheric pressure driven by an electric field of $E = 1$ MV/cm. In the initial adiabatic polarization stage, an external electric field is applied while maintaining the total entropy of the system constant. The system undergoes a transition from the initial unpolarized and disordered State A to a polarized and ordered State B, resulting in the heating of PTO. The adiabatic temperature change during heating is defined as follows: $\Delta T_{0\rightarrow E} = T_B - T_A = 47.4$ K. The second stage involves the isofield process, where the system exchanges heat with the surroundings under an electric field, leading to a temperature decrement to 800 K. During this process, the system transitions from State B to State C, exhibiting a slightly enhanced polarization. The isothermal entropy change during heating is determined using the following: $\Delta S_{0\rightarrow E} = Q_{BC}/T = -0.628$ eV/K. In the third stage, known as the adiabatic depolarization stage, the electric field is removed while maintaining constant

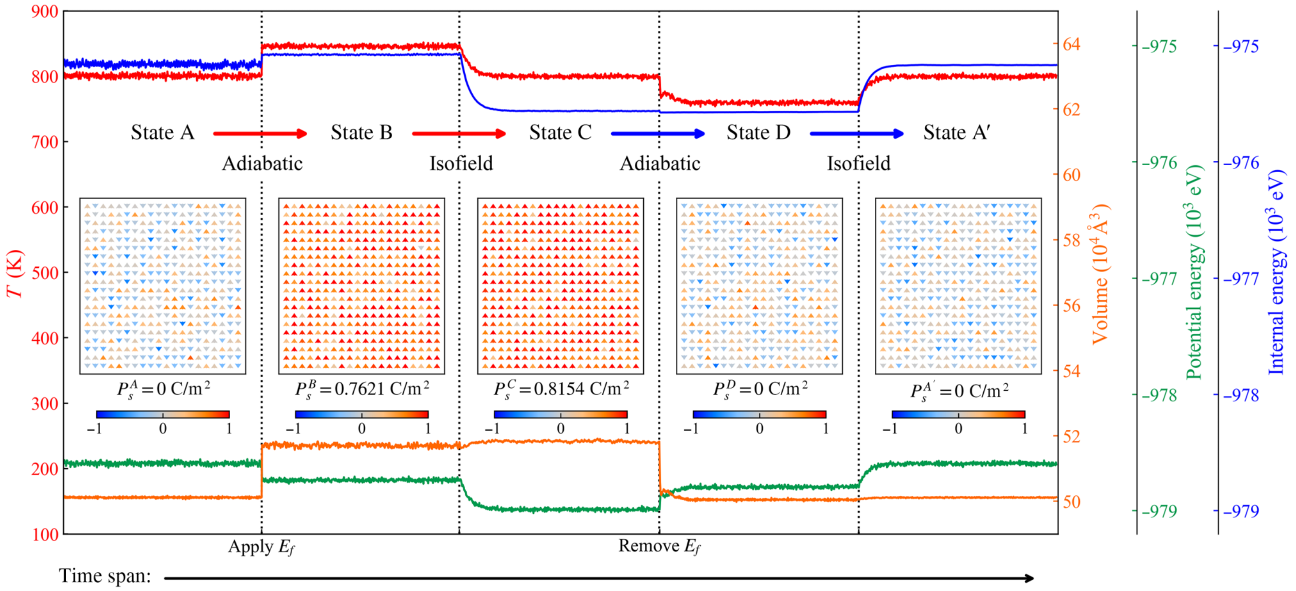

FIG. 4. Process diagram illustrating PbTiO$_3$ electrocaloric refrigeration at 800 K and atmospheric pressure under an electric field of $E = 1$ MV/cm. Red, orange, blue, and green represent variations in temperature, volume, internal energy, and potential energy throughout the entire process. Insets provide microscopic snapshots of the polarization at different states (color bar indicates polarization).

system entropy. The system transitions from the polarized and ordered phase, State C, to the unpolarized and disordered phase, State D, resulting in a decrement of temperature of PTO. The adiabatic temperature change during the cooling is defined as follows: $\Delta T_{E\to 0} = T_D - T_C = -38.2$ K. Finally, the entire process forms a closed loop known as the isofield depolarization stage. Since the working ECE material is colder than the targeted environment, heat is transferred to the ECE material. Simultaneously, the system transitions from State D to State A′. Likely, the isothermal entropy change during cooling is given by $\Delta S_{E\to 0} = Q_{DA'}/T = 0.503$ eV/K. Certainly, we can calculate the identical data using formulas (1) and $\Delta T = -(T/C_T)\Delta S$ so that $\Delta T_{0\to E} = 48.3$ K, $\Delta S_{0\to E} = -0.625$ eV/K, $\Delta T_{E\to 0} = -38.5$ K, and $\Delta S_{E\to 0} = 0.498$ eV/K. This entirely aligns with the results obtained through the direct method.

Using analogous calculations across various temperatures and electric field strengths, one can obtain the temperature-dependent $-\Delta S$ and ΔT under different electric fields, as illustrated in Figs. 5(a) and 5(b). It is evident that as the temperature rises, $-\Delta S_{0\to E}$ shows a positive correlation with the electric field increment. When $T > T_c$, elevating the electric field effectively augments the refrigeration entropy. For instance, at 900 K, the cooling entropy increases from 0 to 14.6 J/(K kg) as the electric field varies from 0.1 MV/cm to 1 MV/cm. However, when $T < T_c$, the impact of the electric field enhancement on cooling entropy is limited. Importantly, $-\Delta S_{E\to 0}$ and $\Delta T_{E\to 0}$ reach their respective maximum values of −21.5 J/(K kg) and −40.5 K at T_c, respectively. It is known that the indirect estimation of ΔS and ΔT, based on the Clausius-Clapeyron and Maxwell relations, are widely used in both experimental and theoretical studies of caloric materials [54–58]. To validate our findings, we employ an indirect method to determine the electric field induced $-\Delta S$ and ΔT, as depicted in Figs. 5(c) and 5(d). A comparison between the outcomes of the applied approach and the conventional indirect method based on Γ_E reveals consistent behavior in the ECE. Specifically, both methods demonstrate an expansion of the cooling temperature range with increasing electric field, extending from 760–800 K for 0.1 MV/cm to 760–900 K for 1 MV/cm. However, due to the inherent challenges in estimating entropy change near a first-order phase transition using indirect methods and the limitations imposed by the interpolation density of Maxwell's differential equations [1], some deviations are observed by comparing the results of these two approaches. The coefficient of performance (COP) stands as a crucial parameter in assessing the efficiency of using caloric materials during the refrigeration process [59]. It is defined as the ratio of the absolute value of cooling capacity to input work, as expressed as either $\eta_{\mathrm{COP}} = |T\Delta S_{E\to 0}|/|W|$ or $\eta_{\mathrm{COP}} = |T\Delta S_{E\to 0}|/|T\Delta S_{0\to E} - T\Delta S_{E\to 0}|$. According to Eq. (1), we can readily derive the dependence of electric field

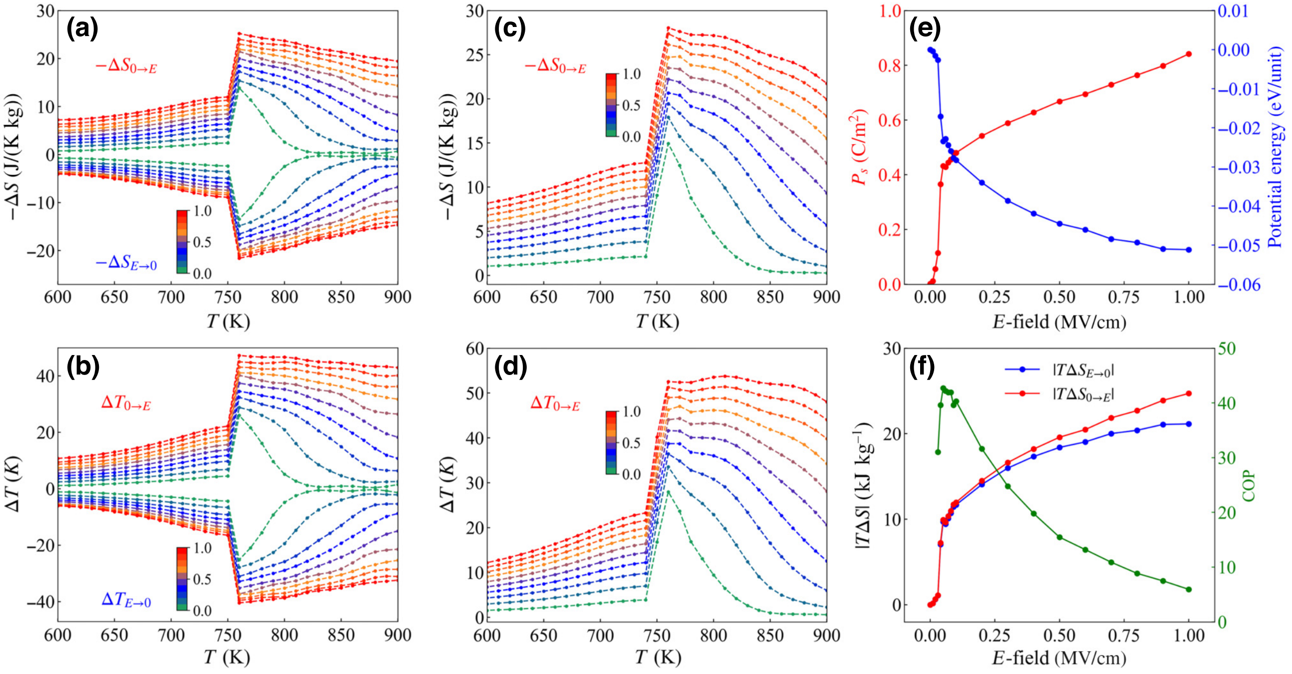

FIG. 5. Temperature-dependent $-\Delta S$ and ΔT under different electric fields calculated by (a),(b) this method and (c),(d) Maxwell's relation (color bar represents electric field ranging from 0 to 1 MV/cm). (e) Curves illustrating the change in polarization (red) and system potential energy (blue) as a function of the electric field at 770 K. (f) Curves depicting the variations of $|\Delta S_{0\to E}|$ (red), $|\Delta S_{E\to 0}|$ (blue), and COP (green) with respect to the electric field at 770 K.

TABLE I. Comparison of the caloric effect between the applied approach and other methods in different types of caloric materials. Time represents the efficiency of calculating the caloric effect in arbitrary units. Here, $\Delta S_{\max}$ is the peak value of isothermal entropy change, Q is the exothermal value, ΔT is the adiabatic temperature change, NPG is the neopentyl glycol, and SGA is the superelastic graphene architectures.

Caloric material	Refrigeration performance						
Electrocaloric $PbTiO_3$	Electric field (kV/cm)	100	200	300	400	500	Time (arb. units)
$\Delta S_{\max}$ (J/(K kg))	This work	13.8	15.4	17.3	18.5	20	1
	Maxwell	14.9	17.9	19.4	20.7	22.2	10–100
Electrocaloric $BaTiO_3$	Electric field (kV/cm)	100	200	300	400	–	Time (arb. units)
Q (J/g)	This work	0.96	2.0	2.2	2.49	–	1
	Exp [60]	1.2	1.7	2.0	2.2	–	–
Magnetocaloric CrI_3	Magnetic field (T)	1	3	5	7	9	Time (arb. units)
$\Delta S_{\max}$ (J/(K kg))	This work	1.45	3.1	4.3	5.23	6.18	1
	Maxwell	1.45	3.3	4.6	5.7	6.7	10–100
	Exp [56]	1.2	2.6	3.8	4.8	5.7	–
Magnetocaloric $CrBr_3$	Magnetic field (T)	1	3	5	7	9	Time (arb. units)
$\Delta S_{\max}$ (J/(K kg))	This work	1.45	3.1	4.3	5.23	6.18	1
	Maxwell	1.45	3.3	4.6	5.7	6.7	10–100
	Exp [57]	1.2	2.6	3.8	4.8	5.7	–
Barocaloric NPG	Pressure (MPa)	0	100	200	300	400	Time (arb. units)
$\Delta S_{\max}$ (J/(K kg))	This work	490	510	550	570	580	1
	Exp [61]	390	425	440	470	510	–
Elastocaloric SGA	Compressive strain	10%	15%	20%	25%	30%	Time (arb. units)
ΔT (K)	This work	30	43	57	73	87	1
	Direct [62]	26	42	58	72	85	>10
Elastocaloric $Ni_{50}Ti_{50}$	Compressive strain	1.25%	1.75%	2%	2.5%	3.25%	Time (arb. units)
ΔT (K)	This work	6	8	9.7	13.6	20	1
	Exp [63]	4	9.6	12.8	17.1	25	–

on COP. Figure 5(e) depicts the potential energy and polarizability at 770 K under different electric fields, while Fig. 5(f) presents the corresponding heat, cooling capacity ($|T\Delta S_{0\to E}|$ and $|T\Delta S_{E\to 0}|$), and COP. From Fig. 5(e), as the electric field increases to 5 MV/m, the polarizability and potential energy exhibit a sudden change, followed by linear variations with the electric field. This sudden change corresponds to the maximum value of the COP, which is 44.

Importantly, this approach for calculating caloric effect is not confined to PTO but can be extended to investigate various field-induced caloric effects in extensive material systems, including magnetocaloric, electrocaloric, elastocaloric, barocaloric, and even multicaloric materials, as shown in Table I; refer to the METHODS section for the specifics. This method excels in evaluating diverse caloric materials' refrigeration capabilities with exceptional performance and reliability. Its efficiency surpasses traditional methods by one to two orders of magnitude, offering a feasible solution for high-throughput screening of high-refrigeration-performance materials (see Appendix A for details).

It is worth noting that Eq. (1) elucidates the fundamental principle of solid-state refrigeration: the transition from a low-potential-energy ordered phase to a high-potential-energy disordered phase requiring heat absorption from the surroundings. Specifically, beyond the Curie temperature ($T > T_c$), State β becomes the ground state. The increment of the external field $\boldsymbol{Y}$ facilitates the transition from State β to State α, leading to a temperature rise ($dT > 0$) and a decrease in entropy ($dS < 0$), as shown in Fig. 6(a). Upon removal of the external field $\boldsymbol{Y}$, the State α spontaneously transitions to State β, absorbing heat and achieving refrigeration, exhibiting conventional caloric effects. Furthermore, this equation also implies the occurrence of the inverse caloric effect, which is observable in various caloric materials including ferroelectrics, ferromagnets, and mechanocaloric materials. If we take external field $\boldsymbol{Y}$ as the driving force for the transition from State β to State α, naturally, $-\boldsymbol{Y}$ serves as the driving force for the transition from State α to State β. Therefore, when the temperature is below the Curie temperature ($T < T_c$), State α becomes the ground state. Increasing the external field $-\boldsymbol{Y}$ pushes State α toward State β, and refrigeration can be achieved if the PED exceeds the input work, representing the inverse caloric effect ($dT < 0$, $dS > 0$), as shown in Fig. 6(b).

Using PTO as an example, State α represents the polarized state, while State β denotes the nonpolarized or weakly polarized state. Here, $\boldsymbol{Y}$ indicates a positive electric field or isotropic tension stress [64], whereas $-\boldsymbol{Y}$ represents a negative electric field or hydrostatic

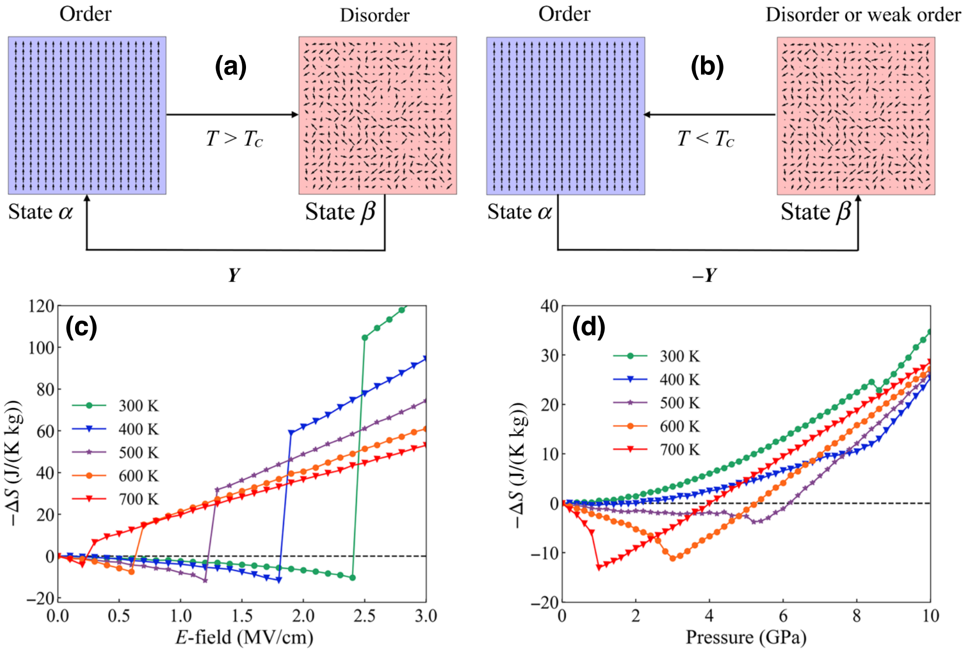

FIG. 6. Schematic diagram of (a) conventional and (b) inverse caloric effects. The isothermal entropy changes of PTO with respect to the (c) inverse electrocaloric and (d) inverse barocaloric effects.

pressure (see Appendix B). In Figs. 6(c) and 6(d), the isothermal entropy change of PTO for the inverse electrocaloric and inverse barocaloric effects are illustrated. As the temperature decreases from 700 to 300 K, $-\Delta S_{\rm max}$ of the inverse electrocaloric effect gradually decreases and approaches saturation at ~ -10.3 J/(K kg). This phenomenon is attributed to the enhanced coercive field of PTO at lower temperatures, resulting in a larger PED between State α and State β. However, as the external field increases, W_Y proportionally increases, ultimately balancing the PED with the work performed by the field. In contrast, the inverse barocaloric effect exhibits a decrement of $-\Delta S_{\rm max}$ near the Curie temperature, reaching a minimum of -13.0 J/(K kg) at 700 K. Nevertheless, as the temperature decreases, $-\Delta S_{\rm max}$ increases gradually and reaches a positive value at 400 K. This occurrence arises from PTO's reduced sensitivity to pressure compared with its response to electric fields, necessitating a substantial amount of work to trigger the phase transition at low temperature, causing $-\Delta S_{\rm max}$ to become positive below 400 K. Table II showcases the inverse caloric effect in electrocaloric, magnetocaloric, and mechanocaloric materials. These results support the proposition that any caloric materials can demonstrate pronounced inverse caloric effects below T_c.

Multicaloric effects in solid-state refrigeration have gained significant attention due to the enhanced ability to control thermal effects by manipulating multiple external fields [65]. Current research on multicaloric effects often requires complex computational procedures, including the integration and differentiation of order parameters with respect to multiple fields [66,67]. In contrast, the PED approach presents a straightforward and efficient approach for investigating multicaloric effects, requiring only the calculation of $\Delta U^{\rm pot}|_{(y_a^0,y_b^0,y_c^0\ldots,T)}^{(y_a^1,y_b^1,y_c^1\ldots,T)}$ and $\sum W_{Y_i}$. Figures 7(a) and 7(b) illustrate a scenario involving a multicaloric process where the electric field varies under an applied

TABLE II. Inverse caloric effect. Here, $\Delta S_{\rm max}$ [J/(K kg)] is the peak value of the isothermal entropy that changes during the field application process ($0 \rightarrow \boldsymbol{Y}$).

Caloric material		Inverse caloric effect				
Electrocaloric	T (K)	300	400	500	600	700
PTO ($T_c = 760$ K)	$\Delta S_{\rm max}$	10.3	11.5	11.2	7.1	4.0
Baroocaloric	T (K)	300	400	500	600	700
PTO ($T_c = 760$ K)	$\Delta S_{\rm max}$	–	–	3.8	11.2	13.0
Magnetocaloric	T (K)	40	45	50	55	60
CrI$_3$ ($T_c = 61$ K) [56]	$\Delta S_{\rm max}$	2.7	2.5	2.3	1.6	0.2
Magnetocaloric	T (K)	20	25	30	35	40
CrBr$_3$ ($T_c = 45$ K) [57]	$\Delta S_{\rm max}$	–	5.5	5.8	5.2	3.7
Mechanocaloric	T (K)	290	295	300	–	–
NPG ($T_c = 315$ K) [61]	$\Delta S_{\rm max}$	231	308	394	–	–

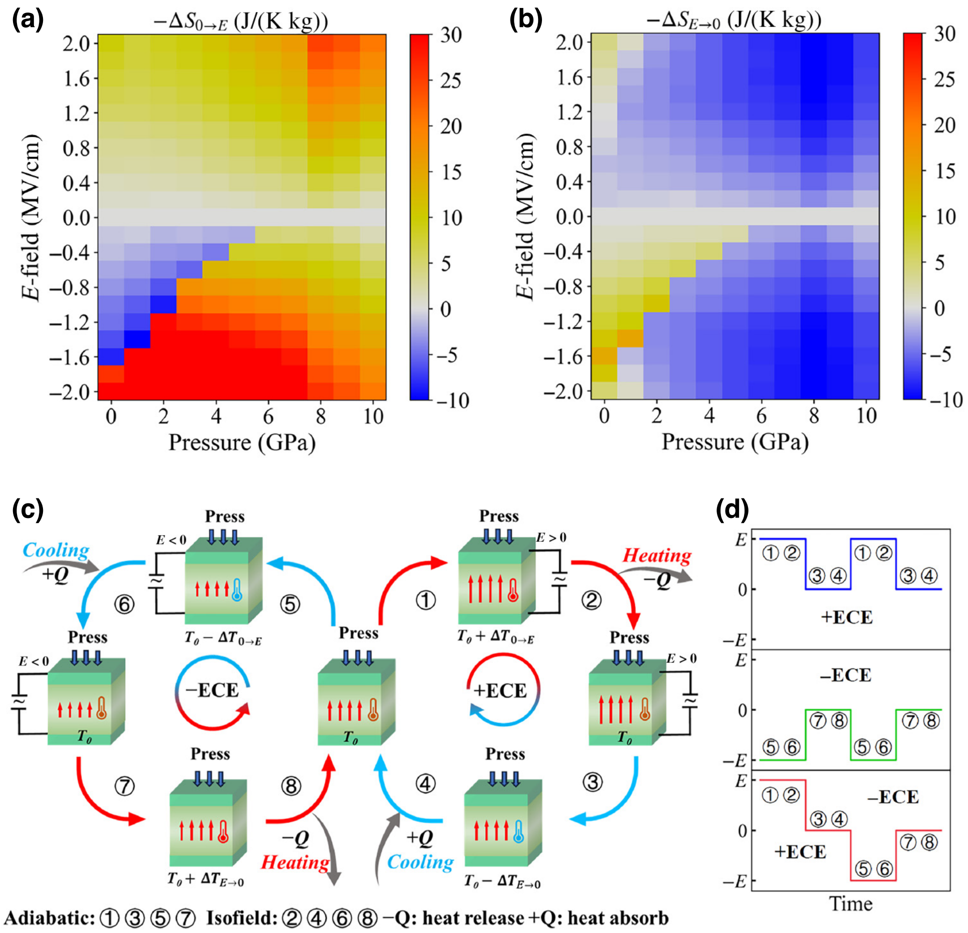

FIG. 7. (a),(b) Isothermal entropy change of applied ($\Delta S_{0\to E}$) or removed ($\Delta S_{E\to 0}$) electric field at 400 K under different pressures. (c) The designed refrigeration cycle (① → ② → ③ → ④ → ⑤ → ⑥ → ⑦ → ⑧ → ①) that combines both conventional (① → ② → ③ → ④ → ①) and inverse (⑤ → ⑥ → ⑦ → ⑧ → ⑤) caloric effect. (d) Schematic diagram of the periodic pulse of the applied electric field, with the blue, green, and red lines representing the conventional, inverse, and designed refrigeration cycle, respectively.

mechanical field. For pressures below 6 GPa, increasing pressure enhances the inverse caloric effect, leading to increased entropy under the same negative electric field. One may note that the inverse caloric effect disappears gradually under higher pressure exceeding 7 GPa, where the ground state shifts from a polarized to a nonpolar state, as shown in Fig. 7(a). In the case of the conventional caloric effect, increasing pressure enhances cooling entropy, reaching its maximum at 8 GPa, as shown in Fig. 7(b).

The established two-dimensional phase diagram of the multicaloric effect can be utilized to optimize the maximum refrigeration performance. Through proper control of the electric field and pressure, one can significantly enhance the cooling performance in one refrigeration cycle under the same pressure via synergistic regulating of the conventional and inverse caloric effect. As illustrated in Figs. 7(c) and 7(d), in one periodic pulse of applied electric field, the refrigeration cycle encompasses two cooling stages, ③ → ④ and ⑤ → ⑥, corresponding to conventional (① → ② → ③ → ④ → ①) and inverse (⑤ → ⑥ → ⑦ → ⑧ → ⑤) caloric effect, respectively. Significantly, the refrigeration cycle remarkably outperforms a single process of conventional ECE in terms of efficiency. For instance, at 400 K under a pressure of 2 GPa, the total cooling effect ($\Delta S_{\text{total}} = \Delta S_{(1.2\ \text{MV/cm})\to 0} + \Delta S_{0\to(-1\ \text{MV/cm})} = 12.3$ J/(K kg)) is more than three times higher than that in the single conventional ECE ($\Delta S_{(1.2\ \text{MV/cm})\to 0} = 3.6$ J/(K kg)).

III. METHODS

A. General approach

In this research, we propose to calculate the caloric effect in various caloric materials by solely requiring the potential energy difference between the initial and final states, as well as the work done by an external field.

Firstly, we derive the essential expressions for adiabatic temperature change and isothermal entropy change with the consideration of external input work and internal kinetic and potential energy. These derivations are rooted in the fundamental principles of the first law of thermodynamics, i.e.,

$$dU = đW + đQ, \tag{2}$$

where dU represents the total differential of internal energy, $đW = Ydy$ denotes the infinitesimal work, and $đQ$ corresponds to heat transfer with surroundings, expressed as TdS. Notably, $\boldsymbol{Y}$ signifies the generalized force (external field), and y denotes the generalized coordinates (the order parameter). Therefore, we have

$$TdS = dU - Ydy. \tag{3}$$

Since S is a state function, by isolating dS and integrating the preceding equation, we can determine the entropy change between two states (T_0, y_0) and (T_1, y_1) along any path connecting these states so that

$$S(T_1, y_1) - S(T_0, y_0) = \frac{\int_{(T_0,y_0)}^{(T_1,y_1)} dU - \int_{(T_0,y_0)}^{(T_1,y_1)} Ydy}{T}. \tag{4}$$

Using Eq. (4), isothermal entropy change occurring upon an external field change from y_0 to y_1 can be calculated by imposing $T_0 = T_1$, obtaining

$$\Delta S(T, y_0 \to y_1) = \frac{U(T, y_1) - U(T, y_0) - \int_{y_0}^{y_1} Ydy}{T}. \tag{5}$$

The internal energy of a system can be regarded as the combination of interatomic potential energy and atomic kinetic energy: $U = U^{\text{pot}} + U^{\text{kin}}$. When two states share the same temperature, their kinetic energy is also identical, thus,

$$\Delta S(T, y_0 \to y_1) = \frac{\Delta U^{\text{pot}}|_{y_0}^{y_1} - W_Y}{T}, \tag{6}$$

where $\Delta U^{\text{pot}}|_{y_0}^{y_1} = U_{y_1}^{\text{pot}} - U_{y_0}^{\text{pot}}$, and W_Y is the work done by the external field.

Let us examine the adiabatic process with entropy change $\Delta S = 0$ and introduce an intermediate state (T_0, y_1), then Eq. (4) can be rewritten as

$$\int_{(T_0,y_0)}^{(T_0,y_1)} dU + \int_{(T_0,y_1)}^{(T_1,y_1)} dU = \int_{(T_0,y_0)}^{(T_1,y_1)} Ydy. \tag{7}$$

According to the thermodynamic relations $\int_{T_0}^{T_1} đQ = \int_{T_0}^{T_1} C_{y_1} dT$ and $đW = Ydy$, Eqs. (2) and (7) can be simplified as follows:

$$\int_{T_0}^{T_1} C_{y_1} dT = \int_{(T_0,y_0)}^{(T_1,y_1)} Ydy - \int_{T_0}^{T_1} (Ydy)_{y_1} - \int_{(T_0,y_0)}^{(T_0,y_1)} dU. \tag{8}$$

In Eq. (8), two approximations are employed: first, C_{y_1} is assumed to be independent of temperature and equal to heat capacity at T_0; second, when calculating work, the state (T_0, y_1) is taken as the intermediate state, then $\int_{(T_0,y_0)}^{(T_1,y_1)} Ydy = \int_{y_0}^{y_1} (Ydy)_T + \int_{T_0}^{T_1} (Ydy)_{y_1}$. Accordingly, Eq. (8) results in the following expression for the adiabatic temperature change:

$$\Delta T(T, y_0 \to y_1) \simeq -\frac{T}{C_y} \Delta S(T, y_0 \to y_1). \tag{9}$$

B. Deep potential

In this study, we utilized a closed-loop automated approach to train the deep potential of PTO employing the deep potential generator (DP-GEN) [35]. The DP-GEN method involves a series of iterations, each comprising three steps: training, exploration, and labeling. We briefly discuss the key concepts in the DP-GEN and DeeP molecular dynamics (MD) and refer interested readers to the original papers [35–37] for detailed discussions. Here, $E_\omega(R)$ (abbreviated to E_ω) represents the potential energy surface (PES) in the DP model, where R denotes atomic positions and ω denotes the parameters. An important point throughout the DP-GEN procedure is that we have a series of models $\{E_{\omega 1}, E_{\omega 2}, \ldots, E_{\omega\alpha}, \ldots\}$ trained from the same set of data but with a difference in the initialization of the model parameters ω_α. In addition, ω_α evolves during the training process, which is designed to minimize the loss function ($\min L(p_\varepsilon, p_f, p_\xi)$), a measure of the error between the DP model and density functional theory results for the energies, forces, and virial tensors. The explicit form of L, defined as a sum of different mean square errors of the deep neural network predictions, is written as

$$L(p_\epsilon, p_f, p_\xi) = \frac{p_\epsilon}{N} \Delta E^2 + \frac{p_f}{3N} \sum_i |\Delta \boldsymbol{F}_i|^2 + \frac{p_\xi}{9N} \parallel \Delta \Xi \|^2, \tag{10}$$

where ΔE, ΔF_{i}, and $\Delta \Xi$ represent the root mean square error in the energy, force, and virial tensors, respectively. The prefactors p_ϵ, p_f, and p_ξ are free to change even during the optimization process. These are given by

$$p(t) = p^{\text{limit}} \left[1 - \frac{r_l(t)}{r_l^0}\right] + p^{\text{start}} \left[\frac{r_l(t)}{r_l^0}\right], \tag{11}$$

where $r_l(t)$ and r_l^0 are the learning rate at training step t and the learning rate at the beginning, respectively. The prefactor varies from p^{start} at the beginning and moves to p^{limit} as the learning ends. We adopt an exponentially decaying learning rate, i.e.,

$$r_l(t) = r_l^0 d_r^{t/d_s}, \tag{12}$$

where d_r and d_s are the decay rate and decay steps, respectively. The decay rate d_r is required to be less than 1.

Since the loss function is a nonconvex function of ω, such a difference in initialization leads to different minimizers after training and, therefore, different PES models. Around configurations where there is sufficient training data, the different PES models should all be fairly accurate and, therefore, produce predictions that are close to each other. Otherwise, one would expect that the predictions from the different models will scatter with a considerable variance. Hence, the variance of the ensemble of predictions from random seed models for a particular configuration can be used as an error indicator and criterion for whether the configuration should be selected for labeling.

In practice, we define the model deviation, ϵ_t, as the maximum standard deviation of the predictions for the atomic forces, i.e.,

$$\epsilon_t = \max_i \sqrt{\langle \| \boldsymbol{f}_i - \bar{\boldsymbol{f}}_i \|^2 \rangle}, \; \bar{\boldsymbol{f}}_i = \langle \boldsymbol{f}_i \rangle, \tag{13}$$

where i runs through the atomic indices in a configuration and the ensemble average $\langle \ldots \rangle$ is taken over the random seed models. For $\epsilon_t < \sigma_{\text{lo}}$, many of the explored configurations can be predicted with high accuracy by the DP models. For $\sigma_{\text{hi}} \le \epsilon_t$, the exploration is driven by a relatively poor model. The upper bound of trust level σ_{hi} is set to exclude the unphysical configurations from the labeling stage to prevent numerical difficulties in the first-principles calculations and to save on computational costs. A rule of thumb setting of σ_{hi} is 0.15–0.30 eV/Å, which is higher than σ_{lo}. When $\sigma_{\text{lo}} \le \epsilon_t < \sigma_{\text{hi}}$, based on the reasoning above, structures corresponding to this situation are selected as candidates for labeling.

In the initial datasets and labeling step, the *ab initio* calculations of the energy, force, and virial were performed using the Vienna *ab initio* Simulation Package (VASP) [68], with the strongly constrained and appropriately normed (SCAN) meta-generalized gradient approximation (meta-GGA) functional [69]. To achieve convergence of the energy and atomic force, an energy cutoff of 500 eV and a k-point spacing of 0.35 Å^{-1} were utilized. The self-consistent field iteration was halted when the difference in total energy was less than 10^{-6} eV.

In the training step, four DP models were trained using the DeePMD-kit software package [36]. The models shared the same set of hyperparameters, but the random seed used to initialize the parameters was different for each model. The size of the embedding net was set at (25, 50, 100), while the fitting net was taken as (240, 240, 240). A cutoff radius of 7 Å and a smoothing parameter of rcut_smth = 0.5 Å were used. The stochastic gradient descent scheme ADAM was employed with a total of 4×10^5 training steps. The hyperparameters start-pref_e, start-pref_f, start-pref_v, limit-pref_e, limit-pref_f, and limit-pref_v were set at 0.01, 100, 0.01, 1.0, 1.0, and 1.0, respectively, to control the weights of the energy and force losses in the total loss function. The starting learning rate was 10^{-3}, which exponentially decayed to 10^{-7} at the end of the training step.

During the exploration step, relevant configurations of a thermodynamic state set that spans a region of the phase diagram are sampled using isothermal-isobaric (NPT) DPMD simulations. The set of initial configurations used in the simulations included the P4mm and Fm-3m phases of the $2 \times 2 \times 2$ and $3 \times 3 \times 3$ supercells, with temperatures ranging from 300 to 900 K, pressure ranging from 1 atm to 5 GPa, and time ranging from 2 ps to 20 ps. The DP-GEN algorithm is executed for a total of 16 iterations. Configurations along the DPMD trajectories are chosen for labeling only if their model uncertainty falls between two predefined trust levels, represented by σ_{lo} and σ_{hi}. The model uncertainty is quantified as the maximum standard deviation of force predicted by a set of DP models that were trained using the same dataset and hyperparameters but initialized with different random seeds. For all 16 iterations, the trust levels are set to $\sigma_{\text{lo}} = 0.07$ and $\sigma_{\text{hi}} = 0.15$ eV Å^{-1}. The final errors between the four models should be smaller than σ_{lo} for all configurations, indicating that the training set is sufficiently considered. Finally, the training set is retrained with larger training steps (10^6) to obtain the ultimate DP model.

C. Electrocaloric effect

After achieving convergence in the DP-GEN iteration, the optimized $PbTiO_3$ DP model can be employed to study polarization changes under varying conditions of temperature, pressure, strain, and electric field through MD simulations conducted using LAMMPS [47]. After reaching thermal equilibrium, the polarization of the system can be calculated using the definition of the Born effective charges,

$$\left(Z_{ij}^* = \frac{V}{e} \frac{\delta P_i}{\delta d_j} \right),$$

in modern polarization theory [38] so that

$$\boldsymbol{P} = \frac{e}{V} \boldsymbol{Z}^* \times \delta \boldsymbol{d} \equiv \begin{pmatrix} P_x \\ P_y \\ P_z \end{pmatrix} = \frac{e}{V} \begin{pmatrix} Z_{xx}^* & Z_{xy}^* & Z_{xz}^* \\ Z_{yx}^* & Z_{yy}^* & Z_{yz}^* \\ Z_{zx}^* & Z_{zy}^* & Z_{zz}^* \end{pmatrix} \begin{pmatrix} \delta d_x \\ \delta d_y \\ \delta d_z \end{pmatrix}, \tag{14}$$

where $\boldsymbol{P}$ represents the polarization intensity, $\boldsymbol{Z}^*$ is the Born effective charge tensor, V is the volume of the cell, and $\delta \boldsymbol{d}$ is the displacement relative to the nonpolarized phase of the atoms. Using another definition of the Born effective charge ($Z^*_{ij} = -(\delta F_i / e \delta E_j)$), we can obtain the effect of an external electric field on the system as follows:

$$\boldsymbol{F} = -e\boldsymbol{Z}^* \times \boldsymbol{E}$$

$$\equiv \begin{pmatrix} F_x \\ F_y \\ F_z \end{pmatrix} = -e \begin{pmatrix} Z^*_{xx} & Z^*_{xy} & Z^*_{xz} \\ Z^*_{yx} & Z^*_{yy} & Z^*_{yz} \\ Z^*_{zx} & Z^*_{zy} & Z^*_{zz} \end{pmatrix} \begin{pmatrix} E_x \\ E_y \\ E_z \end{pmatrix}. \quad (15)$$

Here, $\boldsymbol{E}$ represents the external electric field and $\boldsymbol{F}$ represents the additional force exerted on the atoms due to an external electric field.

Using a $PbTiO_3$-optimized DP model, we performed MD simulations to investigate polarization transitions driven by temperature and electric fields. A supercell (consisting of 5000 atoms) of the polarized phase (the $10 \times 10 \times 10$ supercell) was simulated under periodic boundary conditions using NPT MD (employing the Nosé–Hoover thermostat to control the temperature) at atmosphere pressure to study the polarization transitions under a certain temperature and an applied electric field. The simulation was conducted with a time step of 1 fs, and the total simulation time was set as 20 ps to ensure structural convergence and stability. Similar results were obtained in separated simulations with a $20 \times 20 \times 20$ supercell (consisting of 40 000 atoms).

The indirect approach, on the other hand, utilizes the Maxwell thermodynamic relation $(\partial S/\partial E)_T = (\partial P_s/\partial T)_E$ to determine ΔT and ΔS. In this method, ΔT can be determined by the following expression:

$$\Delta T = -\int_{E_1}^{E_2} \frac{T}{C(E,T)} \left(\frac{\partial P_s}{\partial T}\right)_E dE, \quad (16)$$

while ΔS can be determined via

$$\Delta S = \int_{E_1}^{E_2} \left(\frac{\partial P_s}{\partial T}\right)_E dE, \quad (17)$$

where T is the temperature, P_s is the polarization, and $C(E, T)$ is the specific heat capacity. In addition to the indirect method based on the Maxwell relation, the Clausius-Clapeyron method can also be used to determine the latent heat of the first-order phase transition, which is not included in the Maxwell relation equation. This method uses the equation $\Delta S = \rho \Delta P_0 (dE/dT_0)$, where ΔP_0 represents the polarization change during the phase transition, ρ is density, and T_0 is the phase-transition temperature for different fields. Based on the entropy changes and specific heat capacity, we estimate the adiabatic temperature via the formula $\Delta T = -T\Delta S/C_E$.

D. Magnetocaloric effect

In order to calculate the temperature-dependent demagnetization curves of magnets, the atomistic spin model is utilized that is based on the classic spin Hamiltonian, that is,

$$\mathcal{H} = -\sum_{i<j} J_{ij} \boldsymbol{S}_i \cdot \boldsymbol{S}_j - k_2 \sum_i S_z^2 - \mu_S \sum_i \boldsymbol{B}_{\mathrm{app}} \cdot \boldsymbol{S}_i, \quad (18)$$

the successive terms of which describe the exchange, uniaxial anisotropy, and applied field contributions, respectively. The important parameters are the Heisenberg exchange J_{ij}, the anisotropy constant k_2, and the atomic spin moment μ_S. Moreover, $\boldsymbol{S}_i$ is a unit vector that describes the orientation of the local spin moment and $\boldsymbol{B}_{\mathrm{app}}$ is an externally applied field. In most magnetic materials, the exchange interactions are the dominant contribution, usually by two orders of magnitude, which gives rise to the atomic ordering of the spin directions. For ferromagnetic materials (parallel alignments of the spins) $J_{ij} > 0$, while for antiferromagnetic materials (antiparallel alignments of the spins) $J_{ij} < 0$. The exchange constant can be calculated by combining VASP with WANNIER90 [70] and TB2J [71], while the uniaxial anisotropy is calculated via the difference of total energies with the spin quantization axis aligned along different crystallographic axes. After the parameters were obtained from *ab initio* calculations, the parameterized atomistic spin model was used to perform simulations by using VAMPIRE [72]. The Monte Carlo method was adopted to acquire T_c. After executing 10 000 steps at each temperature, the system of $19\times$ $19\times$ 8 unit cells with in-plane periodic boundary conditions reaches its equilibrium. Then, a statistical average was taken over a further 10 000 steps to extract the mean magnetization. The temperature-dependent magnetization curves were calculated by using the spin dynamics approach and the Heun integration scheme [72]. The demagnetization field induced by the atomistic spins themselves was also included. The external magnetic field was gradually increased to 9 T with an incremental step of 0.1 T.

Simulations at all (H, T) points of interest yield potential energy under any temperature and magnetic field: $Ep = E_T – E_H$, where E_T is the total energy and E_H is the applied field energy. To compute the refrigeration entropy during demagnetization, the results of which are displayed in Table I, we substitute initial and final state potential energies into Eq. (6) so that

$$\Delta S(T_0, H_0 \to 0) = \frac{E_p(T_0, 0) - E_p(T_0, H_0)}{T_0}. \quad (19)$$

If the external magnetic field remains fixed while changing the temperature, the maximum entropy change value

$\Delta S_{\max}$ at that magnetic field H_0 can be obtained. Certainly, to calculate the refrigeration entropy when applying a magnetic field, the results of which are displayed in Table II, the external magnetic field work W_H must be considered. Without flipping the magnetic moments, it can be approximated as $(1/2)\Delta M \times H$, where M is the magnetic moment. Thus, the entropy change is given as

$$\Delta S(T_0, 0 \to H_0) = \frac{E_p(T_0, H_0) - E_p(T_0, 0) - (1/2)\Delta M \times H_0}{T_0}. \quad (20)$$

E. Barocaloric effect

Molecular dynamics simulations under the NPT canonical ensemble were conducted using LAMMPS. Temperature and pressure were controlled using barostatting and thermostatting techniques. The latest version of the COMPASS [73,74] potential was applied in the neopentyl glycol (NPG) simulation. Long-range van der Waals and Coulomb interactions were computed using a particle–particle particle-mesh k-space solver. An integration was performed using the VERLET algorithm with a time step of 1 fs. Each (P, T) point was simulated for 20 ns, and the thermodynamic quantities of the system were statistically averaged over the last 3 ns.

Simulating all (P, T) points of interest allows us to obtain potential energy E_p at any temperature and pressure from the output files. To compute the refrigeration entropy during pressure removal, we substitute the initial and final state potential energies into Eq. (6) so that

$$\Delta S(T_0, P_0 \to 0) = \frac{E_p(T_0, 0) - E_p(T_0, P_0)}{T_0}. \quad (21)$$

Of course, when calculating the refrigeration entropy during the application of pressure, the work done by pressure W_P can be approximated as $(1/2)\Delta V \times P$, where V represents volume. Thus, the entropy change is given as

$$\Delta S(T_0, 0 \to P_0) = \frac{E_p(T_0, P_0) - E_p(T_0, 0) - (1/2)\Delta V \times P_0}{T_0}. \quad (22)$$

F. Elastocaloric effect

MD simulations were conducted using LAMMPS. The adaptive intermolecular reactive empirical bond order potential [75] was utilized to describe carbon–carbon interactions in the superelastic graphene architectures (SGA) simulation. Initially, the model systems were relaxed for 5 ns under an isothermal-isobaric NPT ensemble, where the temperature remained constant at the initial temperature T_0 and the pressure was kept at zero, controlled by the Nosé–Hoover thermostat and barostat. Subsequently, uniaxial tension or compression tests were performed along the carbon nanotubes (CNTs) axis at a strain rate of 0.001 ps^{-1} to obtain the isothermal mechanical properties. The unloading process was conducted by reversing the deformation direction. To account for the large volume change of the entire system during loading and unloading processes and to compute the temperature change ΔT, the NPT ensemble with a large inertial parameter, $T_{\mathrm{damp}} = 10$ ns, was maintained to simulate the adiabatic process by preventing heat transfer between the system and the thermostat. The embedded atom method potential [76] was employed for molecular dynamics simulations of $\mathrm{Ni_{50}Ti_{50}}$, with the other steps being similar to those of SGA for $\mathrm{Ni_{50}Ti_{50}}$.

Simulating all (σ, T) points of interest allows us to obtain potential energy at any temperature and strain from the output files. In this paper, we only considered the refrigeration entropy during strain recovery. Thus, by substituting the initial and final state energies into Eq. (6), we obtain the following expression:

$$\Delta S(T_0, \sigma_0 \to 0) = \frac{E_p(T_0, 0) - E_p(T_0, \sigma_0)}{T_0}. \quad (23)$$

IV. CONCLUSION

In summary, we propose to apply a potential energy difference to investigate the fundamental refrigeration parameters under an external field that can be applied to a variety of caloric materials. This reveals that the refrigeration process involves heat absorption by a transition from a low-potential-energy to a high-potential-energy state, which can be driven either by a temperature change or an external field. This approach enables efficient determination of refrigeration parameters that offer significant advantages for machine-learning-assisted high-throughput screening of caloric materials with the desired properties. In addition, the design of a combined conventional and inverse caloric cooling cycle shows significant implications for multicaloric solid-state refrigeration technology. Our work provides important insights and feasible strategies to optimize the refrigeration performance of caloric materials for practical applications.

ACKNOWLEDGMENTS

This work was supported by National Natural Science Foundation of China (Grants No. 12174450 and No. 11874429), National Talents Program of China, Hunan Provincial Key Project (Grant No. 2024JJ3029), Leading Talent of Hunan Provincial Technological Innovation, Key Research and Development Program (Grant No. 2022WK2002), Distinguished Youth Foundation (Grant No. 2020JJ2039), Project of High-Level Talents Accumulation (Grant No. 2018RS3021), Program of Hundreds of Talents, State Key Laboratory of Powder Metallurgy, Start-up Funding and Innovation-Driven Plan (Grant No.

2019CX023) of Central South University, Postgraduate Scientific Research Innovation Project of Hunan Province (Grants No. CX20230104 and No. CX20220252). Calculations were performed at high-performance computing facilities of Central South University.

APPENDIX A: COMPUTATIONAL EFFICIENCY

Conventionally, when employing the Maxwell method to compute entropy change, $\Delta S = \int_{E_1}^{E_2} \rho(\partial P_s/\partial T)_E dE$, it is essential to consider at least two data points around the target temperature T_0 in order to numerically calculate $(\partial P_s/\partial T)_E$ using $P(T_0+t) - P(T_0-t)/2t$. When performing numerical integration to compute $\int_{E_1}^{E_2} \rho(\partial P_s/\partial T)_E dE$, it is crucial that dE is sufficiently small. For example, in our paper, we chose $dE = 0.02$ MV/cm. To compute the entropy change from 0 to 1 MV/cm using the Maxwell method, one would require calculating at least 2×50 data points. However, with our method for computing entropy change, we use the following:

$$\Delta S(T, y_0 \to y_1) = \frac{\Delta U^{\text{pot}}|_{y_0}^{y_1} - W_Y}{T},$$

where only two data points are needed, representing the initial and final states. This significantly highlights the advantage in terms of computational efficiency. Furthermore, we investigated the multicaloric effect of PTO at 400 K, as depicted in Fig. 7. If we were to compute the entropy change in Fig. 7 using the Maxwell method, one would need ($201 \times 11 \times 2 = 4422$) data points. Each data point requires the running of 5000 atoms for 20 000 steps of DP-MD simulation, summing up to a total of 4.422×10^{11} atom steps. At present, the computational speed of four RTX 3090 graphics cards is approximately 2.4×10^5 (atom steps)/s. Consequently, it would take at least 21 days to compute all the data shown in Fig. 7, assuming no errors or data processing overheads. In contrast, one only needs $41 \times 11 = 451$ data points by using the method in the present work. This means we can complete the computation in roughly two days, representing a significant efficiency boost for the multicaloric effects and providing a solid foundation for the high-throughput screening of solid-state refrigeration materials.

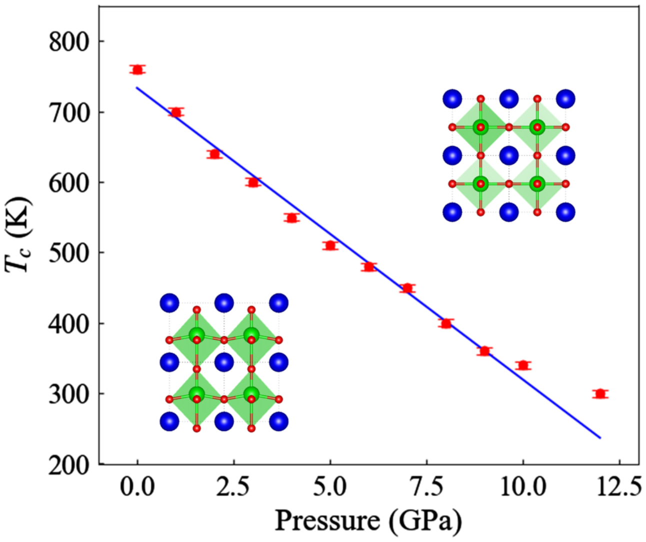

FIG. 8. Pressure-temperature phase diagram of PTO. Insets provide the structure of the P4mm phase and Fm-3m phase.

APPENDIX B: PRESSURE PROMOTES THE PHASE TRANSITION

Figure 8 illustrates the dependence of pressure on Curie temperature T_c, showing that T_c decreases almost linearly with increasing pressure and reaches room temperature at around 12 GPa. The pressure-induced P4mm to Fm-3m phase transition carries the essence of statistical physics. We write the differential equation of $G(p, T)$ for the two phases I (low-temperature phase) and II (high-temperature phase) as follows:

$$dG_{\text{I}} = V_{\text{I}}dp - S_{\text{I}}dT; dG_{\text{II}} = V_{\text{II}}dp - S_{\text{II}}dT. \tag{B1}$$

Considering that through an infinitesimal path along the coexistence curve of these two phases, infinitesimal changes of the Gibbs free energy of each phase must be the same, that is, $dG_{\text{I}} = dG_{\text{II}}$, which results in the following expressions:

$$V_{\text{I}}dp - S_{\text{I}}dT = V_{\text{II}}dp - S_{\text{II}}dT \to (V_{\text{I}} - V_{\text{II}})dp = (S_{\text{I}} - S_{\text{II}})dT, \tag{B2}$$

$$\frac{dT}{dp} = \frac{\Delta V_t}{\Delta S_t} = \frac{T\Delta V_t}{\Delta H_t}, \tag{B3}$$

where dT/dp is the slope of the two-phase coexistence line with $T(p)$ constituting the phase diagram. For PTO, when $\Delta V_t < 0$ and $\Delta S_t = -\int (dV/dT) > 0$, it is implied that $dT/dp < 0$, as shown in Fig. 8, which suggests that the application of hydrostatic pressure on PTO facilitates the P4mm to Fm-3m phase transition.

[1] V. Franco, J. S. Blázquez, J. J. Ipus, J. Y. Law, L. M. Moreno-Ramírez, and A. Conde, Magnetocaloric effect: from materials research to refrigeration devices, Prog. Mater. Sci. **93**, 112 (2018).

[2] S. A. Nikitin, G. Myalikgulyev, A. M. Tishin, M. P. Annaorazov, K. A. Asatryan, and A. L. Tyurin, The magnetocaloric effect in $Fe_{49}Rh_{51}$ compound, Phys. Lett. A **148**, 363 (1990).

[3] A. Edström and C. Ederer, Prediction of a giant magnetoelectric cross-caloric effect around a tetracritical point in multiferroic $SrMnO_3$, Phys. Rev. Lett. **124**, 167201 (2020).

[4] S. Gama, A. A. Coelho, A. de Campos, A. M. G. Carvalho, F. C. G. Gandra, P. J. von Ranke, and N. A. de Oliveira, Pressure-induced colossal magnetocaloric effect in MnAs, Phys. Rev. Lett. **93**, 237202 (2004).

[5] V. K. Pecharsky and K. A. Gschneidner Jr., Giant magnetocaloric effect in $Gd_5(Si_2Ge_2)$, Phys. Rev. Lett. **78**, 4494 (1997).

[6] S. Yu. Dan'kov, A. M. Tishin, V. K. Pecharsky, and K. A. Gschneidner, Magnetic phase transitions and the magnetothermal properties of gadolinium, Phys. Rev. B **57**, 3478 (1998).

[7] H. Wada and Y. Tanabe, Giant magnetocaloric effect of $MnAs_{1-x}Sb_x$, Appl. Phys. Lett. **79**, 3302 (2001).

[8] A. S. Mischenko, Q. Zhang, J. F. Scott, R. W. Whatmore, and N. D. Mathur, Giant electrocaloric effect in thin-film $PbZr_{0.95}Ti_{0.05}O_3$, Science **311**, 1270 (2006).

[9] A. Torelló and E. Defay, Electrocaloric coolers: a review, Adv. Electron. Mater. **8**, 2101031 (2022).

[10] J. Shi, D. Han, Z. Li, L. Yang, S.-G. Lu, Z. Zhong, J. Chen, Q. M. Zhang, and X. Qian, Electrocaloric cooling materials and devices for zero-global-warming-potential, high-efficiency refrigeration, Joule **3**, 1200 (2019).

[11] J. F. Scott, Electrocaloric materials, Annu. Rev. Mater. Res. **41**, 229 (2011).

[12] Electrocaloric materials for future solid-state refrigeration technologies, Prog. Mater. Sci. **57**, 980 (2012).

[13] I. Ponomareva and S. Lisenkov, Bridging the macroscopic and atomistic descriptions of the electrocaloric effect, Phys. Rev. Lett. **108**, 167604 (2012).

[14] M. C. Rose and R. E. Cohen, Giant electrocaloric effect around T_c, Phys. Rev. Lett. **109**, 187604 (2012).

[15] D. Cong, W. Xiong, A. Planes, Y. Ren, L. Mañosa, P. Cao, Z. Nie, X. Sun, Z. Yang, X. Hong, *et al.*, Colossal elastocaloric effect in ferroelastic Ni-Mn-Ti alloys, Phys. Rev. Lett. **122**, 255703 (2019).

[16] E. Bonnot, R. Romero, L. Mañosa, E. Vives, and A. Planes, Elastocaloric effect associated with the martensitic transition in shape-memory alloys, Phys. Rev. Lett. **100**, 125901 (2008).

[17] M. P. Annaorazov, S. A. Nikitin, A. L. Tyurin, K. A. Asatryan, and A. Kh. Dovletov, Anomalously high entropy change in FeRh alloy, J. Appl. Phys. **79**, 1689 (1996).

[18] J. Cui, Y. Wu, J. Muehlbauer, Y. Hwang, R. Radermacher, S. Fackler, M. Wuttig, and I. Takeuchi, Demonstration of high efficiency elastocaloric cooling with large ΔT using NiTi wires, Appl. Phys. Lett. **101**, 073904 (2012).

[19] L. Mañosa and A. Planes, Materials with giant mechanocaloric effects: cooling by strength, Adv. Mater. **29**, 1603607 (2017).

[20] K. Tao, W. Song, J. Lin, X. Zhang, P. Tong, Z. Zhang, J. Qi, B. Li, L. Ling, L. Ma, *et al.*, Giant reversible barocaloric effect with low hysteresis in antiperovskite $PdNMn_3$ compound, Scr. Mater. **203**, 114049 (2021).

[21] L. Mañosa, D. González-Alonso, A. Planes, E. Bonnot, M. Barrio, J.-L. Tamarit, S. Aksoy, and M. Acet, Giant solid-state barocaloric effect in the Ni–Mn–In magnetic shape-memory alloy, Nat. Mater. **9**, 478 (2010).

[22] F. B. Li, M. Li, X. Xu, Z. C. Yang, H. Xu, C. K. Jia, K. Li, J. He, B. Li, and H. Wang, Understanding colossal barocaloric effects in plastic crystals, Nat. Commun. **11**, 4190 (2020).

[23] B. Li, Y. Kawakita, S. Ohira-Kawamura, T. Sugahara, H. Wang, J. Wang, Y. Chen, S. I. Kawaguchi, S. Kawaguchi, K. Ohara, *et al.*, Colossal barocaloric effects in plastic crystals, Nature **567**, 506 (2019).

[24] Z. Zhang, X. Jiang, T. Hattori, X. Xu, M. Li, C. Yu, Z. Zhang, D. Yu, R. Mole, S. Yano, *et al.*, A colossal barocaloric effect induced by the creation of a high-pressure phase, Mater. Horiz. **10**, 977 (2023).

[25] R. P. Santana, N. A. De Oliveira, and P. J. Von Ranke, Anomalous barocaloric effect in solid magnetic materials, J. Phys.: Condens. Matter **23**, 306003 (2011).

[26] C. Niu, F. Li, X. Xu, W. Xie, G. Zhai, M. Li, and H. Wang, Colossal barocaloric effect of plastic crystals imbedded in silicon frame near room temperature: molecular dynamics simulation, Appl. Phys. Lett. **124**, 103905 (2024).

[27] F. Li, C. Niu, X. Xu, W. Xie, M. Li, and H. Wang, Predicting large comprehensive refrigeration performance of plastic crystals by compositing carbon architectures for room temperature application, Appl. Phys. Lett. **123**, 183902 (2023).

[28] F. Li, C. Niu, X. Xu, M. Li, and H. Wang, The effect of defect and substitution on barocaloric performance of neopentylglycol plastic crystals, Appl. Phys. Lett. **121**, 223902 (2022).

[29] F. Li, M. Li, C. Niu, and H. Wang, Atomic-scale insights into the colossal barocaloric effects of neopentyl glycol plastic crystals, Appl. Phys. Lett. **120**, 073902 (2022).

[30] X. Moya and N. D. Mathur, Caloric materials for cooling and heating, Science **370**, 797 (2020).

[31] Y. Liu, J. F. Scott, and B. Dkhil, Direct and indirect measurements on electrocaloric effect: recent developments and perspectives, Appl. Phys. Rev. **3**, 031102 (2016).

[32] M. Sanlialp, V. V. Shvartsman, M. Acosta, B. Dkhil, and D. C. Lupascu, Strong electrocaloric effect in lead-free $0.65Ba(Zr_{0.2}Ti_{0.8})O_3$–$0.35(Ba_{0.7}Ca_{0.3})TiO_3$ ceramics obtained by direct measurements, Appl. Phys. Lett. **106**, 062901 (2015).

[33] F. L. Goupil, A. Berenov, A.-K. Axelsson, M. Valant, and N. McN. Alford, Direct and indirect electrocaloric measurements on $\langle 001\rangle$-$PbMg_{1/3}Nb_{2/3}O_3$-$30PbTiO_3$ single crystals, J. Appl. Phys. **111**, 124109 (2012).

[34] F. Le Goupil, J. Bennett, A.-K. Axelsson, M. Valant, A. Berenov, A. J. Bell, T. P. Comyn, and N. McN. Alford, Electrocaloric enhancement near the morphotropic phase boundary in lead-free NBT-KBT ceramics, Appl. Phys. Lett. **107**, 172903 (2015).

[35] Y. Zhang, H. Wang, W. Chen, J. Zeng, L. Zhang, H. Wang, and E. Weinan, DP-GEN: a concurrent learning platform for the generation of reliable deep learning based potential energy models, Comput. Phys. Commun. **253**, 107206 (2020).

[36] H. Wang, L. Zhang, J. Han, and E. Weinan, DeePMD-Kit: a deep learning package for many-body potential energy representation and molecular dynamics, Comput. Phys. Commun. **228**, 178 (2018).

[37] L. Zhang, D.-Y. Lin, H. Wang, R. Car, and E. Weinan, Active learning of uniformly accurate interatomic potentials for materials simulation, Phys. Rev. Mater. **3**, 023804 (2019).

[38] N. A. Spaldin, A beginner's guide to the modern theory of polarization, J. Solid State Chem. **195**, 2 (2012).

[39] A. Togo, L. Chaput, T. Tadano, and I. Tanaka, Implementation strategies in Phonopy and Phono3py, J. Phys.: Condens. Matter **35**, 353001 (2023).

[40] A. Togo, First-principles phonon calculations with Phonopy and Phono3py, J. Phys. Soc. Jpn. **92**, 012001 (2023).

[41] W. Xie, X. Xu, M. Li, and H. Wang, Intrinsic Rashba Effect and anomalous valley Hall effect in one-dimensional magnetic nanoribbon, J. Magn. Magn. Mater. **573**, 170662 (2023).

[42] W. Xie, L. Zhang, Y. Yue, M. Li, and H. Wang, Giant valley polarization and perpendicular magnetocrystalline anisotropy energy in monolayer MX_2(M = Ru, Os;X = Cl, Br), Phys. Rev. B **109**, 024406 (2024).

[43] S. A. Mabud and A. M. Glazer, Lattice parameters and birefringence in $PbTiO_3$ single crystals, J. Appl. Crystallogr. **12**, 49 (1979).

[44] A. Sani, M. Hanfland, and D. Levy, Pressure and temperature dependence of the ferroelectric–paraelectric phase transition in $PbTiO_3$, J. Solid State Chem. **167**, 446 (2002).

[45] A. Sani, M. Hanfland, and D. Levy, The equation of state of $PbTiO_3$ up to 37 GPa: a synchrotron x-ray powder diffraction study, J. Phys.: Condens. Matter **14**, 10601 (2002).

[46] J. A. Sanjurjo, E. López-Cruz, and G. Burns, Pressure dependence of the linewidth of the soft phonons in $PbTiO_3$, Solid State Commun. **48**, 221 (1983).

[47] A. P. Thompson, H. M. Aktulga, R. Berger, D. S. Bolintineanu, W. M. Brown, P. S. Crozier, P. J. In 'T Veld, A. Kohlmeyer, S. G. Moore, T. D. Nguyen, *et al.*, LAMMPS - a flexible simulation tool for particle-based materials modeling at the atomic, meso, and continuum scales, Comput. Phys. Commun. **271**, 108171 (2022).

[48] G. A. Rossetti and N. Maffei, Specific heat study and Landau analysis of the phase transition in $PbTiO_3$ single crystals, J. Phys.: Condens. Matter **17**, 3953 (2005).

[49] P. Jouzdani, S. Cuozzo, S. Lisenkov, and I. Ponomareva, Enhancement of electrocaloric response through quantum effects, Phys. Rev. B **96**, 214107 (2017).

[50] K. Szałowski and T. Balcerzak, Magnetocaloric and electrocaloric properties of the Hubbard pair cluster, J. Magn. Magn. Mater. **527**, 167767 (2021).

[51] A. P. Moina, Negative/positive electrocaloric effect in antiferroelectric squaric acid, J. Appl. Phys. **133**, 094101 (2023).

[52] I. F. Mello, L. Squillante, G. O. Gomes, A. C. Seridonio, and M. de Souza, Griffiths-like phase close to the Mott transition, J. Appl. Phys. **128**, 225102 (2020).

[53] X. Moya, E. Stern-Taulats, S. Crossley, D. Gonzalez-Alonso, S. Kar-Narayan, A. Planes, L. Manosa, and N. D. Mathur, Giant electrocaloric strength in single-crystal BaTiO3, Adv. Mater. **25**, 1360 (2013).

[54] H.-R. Ji, R.-J. Zhou, J. Yao, X.-X. Cao, Z.-Y. Jing, Q. Pan, Z.-J. Feng, Z.-X. Gu, and Y.-M. You, Giant electrocaloric effect in a molecular ceramic, Mater. Horiz. **10**, 869 (2023).

[55] C. Liu, W. Si, C. Wu, J. Yang, Y. Chen, and C. Dames, The ignored effects of vibrational entropy and electrocaloric effect in $PbTiO_3$ and $PbZr_{0.5}Ti_{0.5}O_3$ as studied through first-principles calculation, Acta Mater. **191**, 221 (2020).

[56] Y. Liu and C. Petrovic, Anisotropic magnetocaloric effect in single crystals of CrI_3, Phys. Rev. B **97**, 174418 (2018).

[57] X. Yu, X. Zhang, Q. Shi, S. Tian, H. Lei, K. Xu, and H. Hosono, Large magnetocaloric effect in van der Waals crystal $CrBr_3$, Front. Phys. **14**, 43501 (2019).

[58] P. Vales-Castro, R. Faye, M. Vellvehi, Y. Nouchokgwe, X. Perpiñà, J. M. Caicedo, X. Jordà, K. Roleder, D. Kajewski, A. Perez-Tomas, *et al.*, Origin of large negative electrocaloric effect in antiferroelectric $PbZrO_3$, Phys. Rev. B **103**, 054112 (2021).

[59] X. Moya, E. Defay, V. Heine, and N. D. Mathur, Too cool to work, Nat. Phys. **11**, 202 (2015).

[60] Y. Bai, G.-P. Zheng, K. Ding, L. Qiao, S.-Q. Shi, and D. Guo, The giant electrocaloric effect and high effective cooling power near room temperature for $BaTiO_3$ thick film, J. Appl. Phys. **110**, 094103 (2011).

[61] P. Lloveras, A. Aznar, M. Barrio, Ph. Negrier, C. Popescu, A. Planes, L. Mañosa, E. Stern-Taulats, A. Avramenko, N. D. Mathur, *et al.*, Colossal barocaloric effects near room temperature in plastic crystals of neopentylglycol, Nat. Commun. **10**, 1803 (2019).

[62] Z. Zhao, W. Guo, and Z. Zhang, Room-temperature colossal elastocaloric effects in three-dimensional graphene architectures: an atomistic study, Adv. Funct. Mater. **32**, 2203866 (2022).

[63] J. Tušek, A. Žerovnik, M. Čebron, M. Brojan, B. Žužek, K. Engelbrecht, and A. Cadelli, Elastocaloric effect vs fatigue life: exploring the durability limits of Ni-Ti plates under pre-strain conditions for elastocaloric cooling, Acta Mater. **150**, 295 (2018).

[64] D. G. Schlom and C. J. Fennie, The positives of going negative, Nat. Mater. **14**, 969 (2015).

[65] H. Hou, S. Qian, and I. Takeuchi, Materials, physics and systems for multicaloric cooling, Nat. Rev. Mater. **7**, 633 (2022).

[66] E. Stern-Taulats, T. Castán, A. Planes, L. H. Lewis, R. Barua, S. Pramanick, S. Majumdar, and L. Mañosa, Giant multicaloric response of bulk $Fe_{49}Rh_{51}$, Phys. Rev. B **95**, 104424 (2017).

[67] E. Stern-Taulats, T. Castán, L. Mañosa, A. Planes, N. D. Mathur, and X. Moya, Multicaloric materials and effects, MRS Bull. **43**, 295 (2018).

[68] G. Kresse and J. Furthmüller, Efficient iterative schemes for ab initio total-energy calculations using a plane-wave basis set, Phys. Rev. B **54**, 11169 (1996).

[69] J. Sun, A. Ruzsinszky, and J. P. Perdew, Strongly constrained and appropriately normed semilocal density functional, Phys. Rev. Lett. **115**, 036402 (2015).

[70] G. Pizzi, V. Vitale, R. Arita, S. Blügel, F. Freimuth, G. Géranton, M. Gibertini, D. Gresch, C. Johnson, T. Koretsune, *et al.*, Wannier90 as a community code: new features and applications, J. Phys.: Condens. Matter **32**, 165902 (2020).

[71] X. He, N. Helbig, M. J. Verstraete, and E. Bousquet, TB2J: a Python package for computing magnetic

interaction parameters, Comput. Phys. Commun. **264**, 107938 (2021).

[72] R. F. L. Evans, W. J. Fan, P. Chureemart, T. A. Ostler, M. O. A. Ellis, and R. W. Chantrell, Atomistic spin model simulations of magnetic nanomaterials, J. Phys.: Condens. Matter **26**, 103202 (2014).

[73] H. Sun, COMPASS: an ab initio force-field optimized for condensed-phase applications - overview with details on alkane and benzene compounds, J. Phys. Chem. B **102**, 7338 (1998).

[74] H. Sun, Z. Jin, C. Yang, R. L. C. Akkermans, S. H. Robertson, N. A. Spenley, S. Miller, and S. M. Todd, COMPASS II: extended coverage for polymer and drug-like molecule databases, J. Mol. Model. **22**, 47 (2016).

[75] S. J. Stuart, A. B. Tutein, and J. A. Harrison, A reactive potential for hydrocarbons with intermolecular interactions, J. Chem. Phys. **112**, 6472 (2000).

[76] X. W. Zhou, R. A. Johnson, and H. N. G. Wadley, Misfit-energy-increasing dislocations in vapor-deposited CoFe/NiFe multilayers, Phys. Rev. B **69**, 144113 (2004).